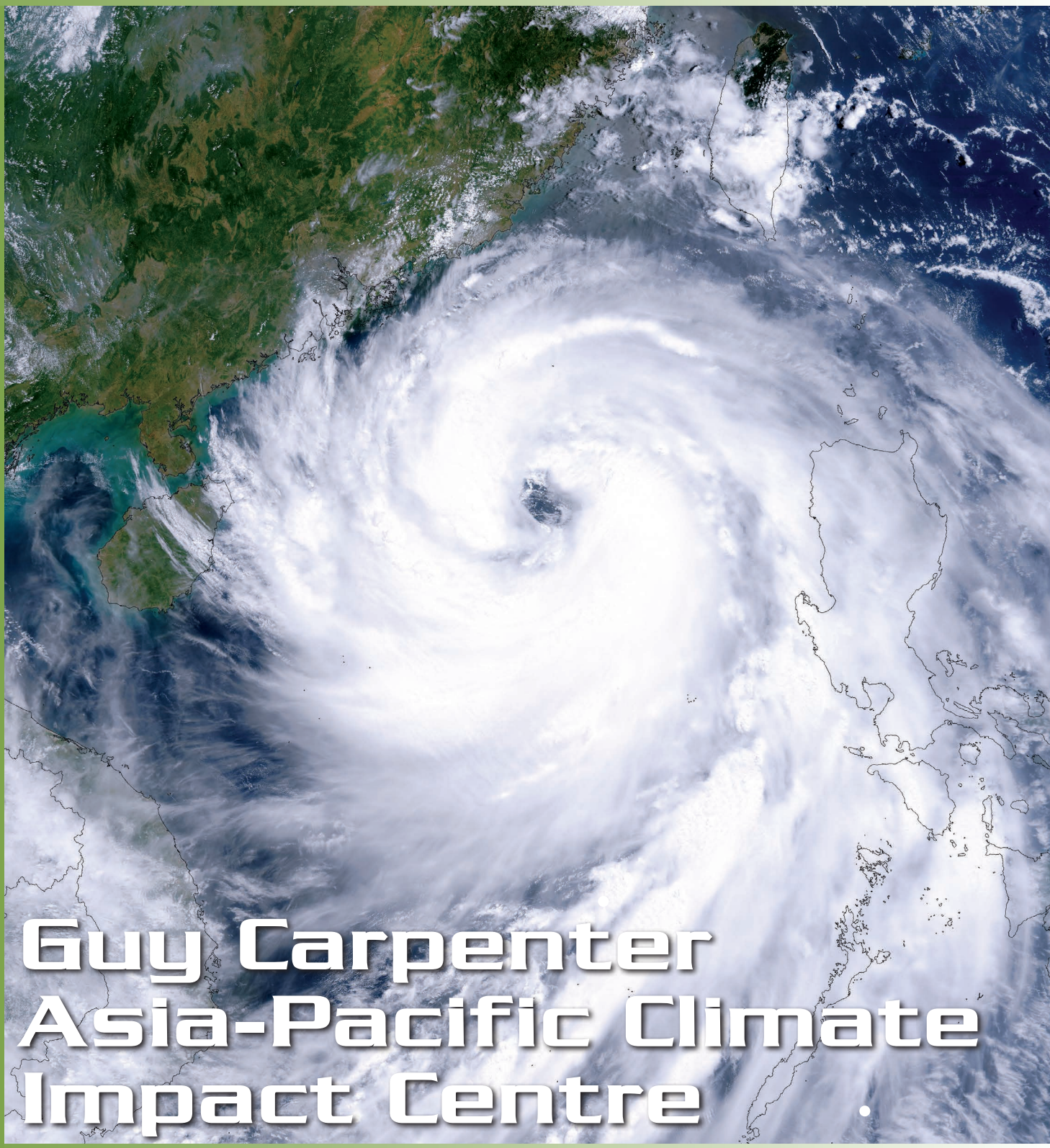

Guy Carpenter Asia-Pacific Climate Impact Centre

Annual Report 2016

GCACIC
Guy Carpenter Asia-Pacific Climate Impact Centre
City University of Hong Kong

CityU
香港城市大學
City University of Hong Kong

Published June 2017

Executive Summary

This is the eighth annual report issued by the Guy Carpenter Asia-Pacific Climate Impact Centre and covers the activities of the Centre in 2016. During the year, we continued to work on improving our understanding of the physical processes responsible for different types of climate variability in our region, which included winter monsoon, regional droughts and heavy precipitation in East Asia. In the area of typhoons, we continue to work on tropical cyclone landfalling activity in East Asia, both of its decadal variation and seasonal forecast. We have been making efforts to improve air pollution measurements and our understanding of Hong Kong air pollution problems based on modelling studies.

The report is divided into five sections, with a total of 15 projects. Section A focuses on climate variability of winter monsoon affecting East Asia, including extreme cold midwinter event, ENSO effect and characteristics of East Asian trough. Section B contains studies related to heavy precipitation and drought problems in China. Section C reports on studies examining the relationship between ENSO and tropical cyclone landfalling activity in South China and the seasonal forecast of that activity using a dynamical model. Section D shows a study investigating the effect of urbanization on precipitation. Section E contains studies related to development of algorithm and error analysis for air sensors and measurement of black carbon and aerosol chemical compositions, as well as air pollution modeling studies related to traffic-related pollutant removal from street canyon with trees, impact of southeast biomass burning on Hong Kong air quality and application of GPS data to mobile estimates.

As in the past, the main results from each of the projects are briefly described in this report. The papers produced from these projects are available either from the CD attached to the report or from our website.

Contents

I. Introduction

The Guy Carpenter Asia-Pacific Climate Impact Centre was established in June 2008. Since 2009, we have been issuing an annual report that describes our research activities during the year, and this is our eighth annual report that describes the activities of the Centre in 2016. During the year, we continued to work on climate problems related to Hong Kong, the Asia-Pacific region as well as those on a global scale, with a total of 15 projects. For each project, we summarise the main results for the reader to have a quick introduction of the subject. In most cases, the results have been published in one or more journal articles, which are listed at the end of the summary of each project. A copy of each of the publications is included in the CD attached to the report and is also available online at http://www.cityu.edu.hk/gcacic/publications.htm.

We hope that this report will provide the reader of an overall picture of the research activities of the Centre. Suggestions and comments on the projects are most welcome.

II. Research Projects

A. Climate Variability

A1. The extreme cold midwinter in 2015/16

(PI: Wen ZHOU)

In January 2016, Asia and North America experienced unusually cold temperatures although the global average surface air temperature broke the warmest record during a strong El Niño event. This extreme cold midwinter was closely related to the remarkable phase transition of the Arctic Oscillation, which can be explained by stratosphere-troposphere interactions. Due to stronger zonal wavenumber 2 signals from the troposphere, the stronger stratospheric polar vortex was elongated, with two cyclonic centers over Asia and the North Atlantic in January (Figure 1). The resultant southward displacement of polar vortices was followed by rare snowfall in the subtropical region of East Asia and a heavy snowstorm on the East Coast of the United States. For more details, please refer to Cheung et al. (2016).

This study investigates the atmospheric conditions responsible for the unusually cold temperatures in Asia and North America in January 2016.

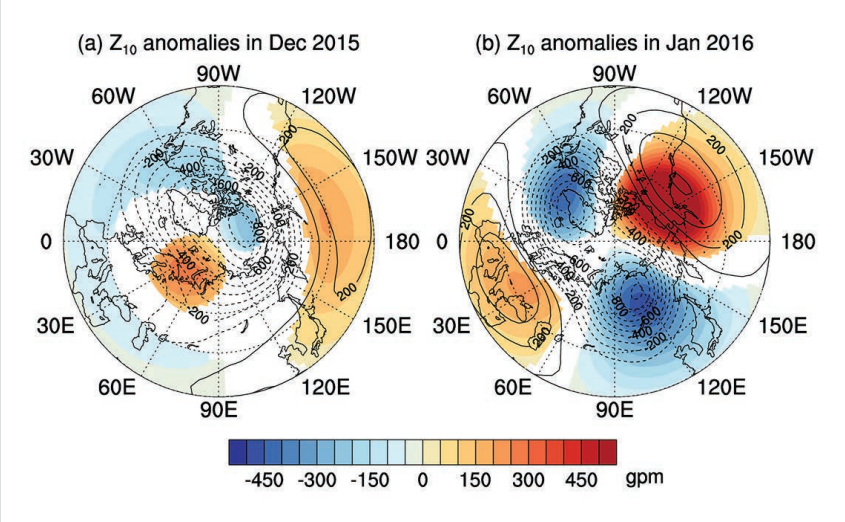

Figure 1. Monthly anomalies of the 10-hPa geopotential height and its zonal wave number 1–3 component (shading) in (a) December 2015 and (b) January 2016. Unit: gpm. The shading represents the values that exceed 0.5σ of the 60year climatological mean. Note that the outermost circle is 30°N.

Reference:

Cheung, H. H. N., W. Zhou, Y. T. Leung, C. M. Shun, S. M. Lee and H. W. Tong, 2016: A strong phase reversal of the Arctic Oscillation in midwinter 2015/16: Role of the stratospheric polar vortex and tropospheric blocking. *Journal of Geophysical Research: Atmospheres*, doi: 10.1002/2016JD025288.

A2. Direct and indirect ENSO modulation of winter temperature

(PI: Wen ZHOU)

The direct and indirect atmospheric responses over the Asian-Pacific-American region to ENSO are documented.

Since El Niño-Southern Oscillation (ENSO) is likely to induce the northward displacement of the East Asian trough (NDEAT), some of the influence of ENSO on the Asian-Pacific-American region is possibly indirect and acts by inducing NDEAT. It is noted that temperature variations in the East Asian-Western Pacific region are controlled mainly by NDEAT. In contrast, ENSO demonstrates a weak direct relation to the temperature variation over the East Asian-Western Pacific region. This suggests that the influence of ENSO on this region is indirect, through modulation of NDEAT. On the other hand, temperature variation over the tropical eastern Pacific is dominated by ENSO forcing (Figure 2). For more details, please refer to Leung and Zhou (2016).

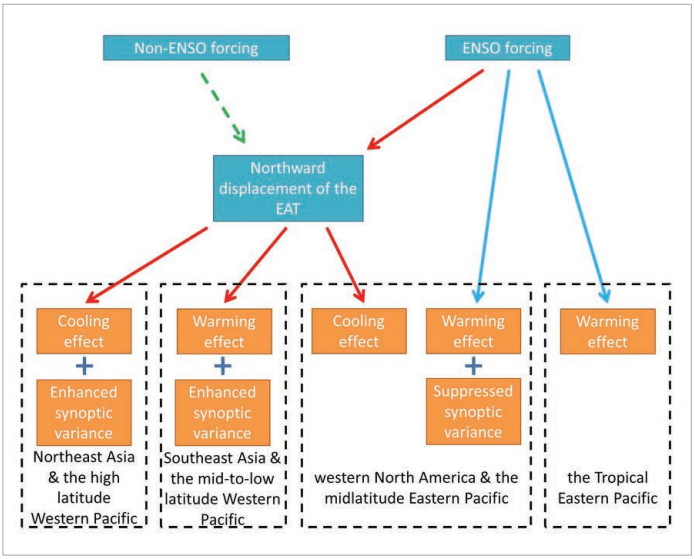

Figure 2. Schematic diagram of the direct (blue arrows) and indirect (red arrows) ENSO forcing on different parts of the Asian-Pacific-American region. The modulation of non-ENSO forcing is indicated with the green dashed arrow.

Reference:

Leung, Y. T. and W. Zhou, 2016: Direct and indirect ENSO modulation of winter temperature over the Asian-Pacific-American region. *Scientific Reports*, doi: 10.1038/srep36356.

A3. East Asian trough and its response to ENSO forcing

(PI: Wen ZHOU)

During the southward displacement of the East Asian trough (EAT), the Siberian high is stronger and the Aleutian low is displaced southward. This is due mainly to the anomalous cyclonic flow associated with seasonal eddies over

the midlatitude central Pacific, which enhances the horizontal advection of cold (warm) air to the southern (northern) part of the EAT in the lower troposphere. The cold (warm) advection reduces (increases) the height thickness and results in negative (positive) temperature anomalies in the southern (northern) part of the EAT (Figure 3). For more details, please refer to Leung et al. (2016).

This study examines the underlying dynamic mechanisms associated with the meridional displacement of the East Asian trough, which is closely related to the temperature variability in the southern part of East Asian winter monsoon.

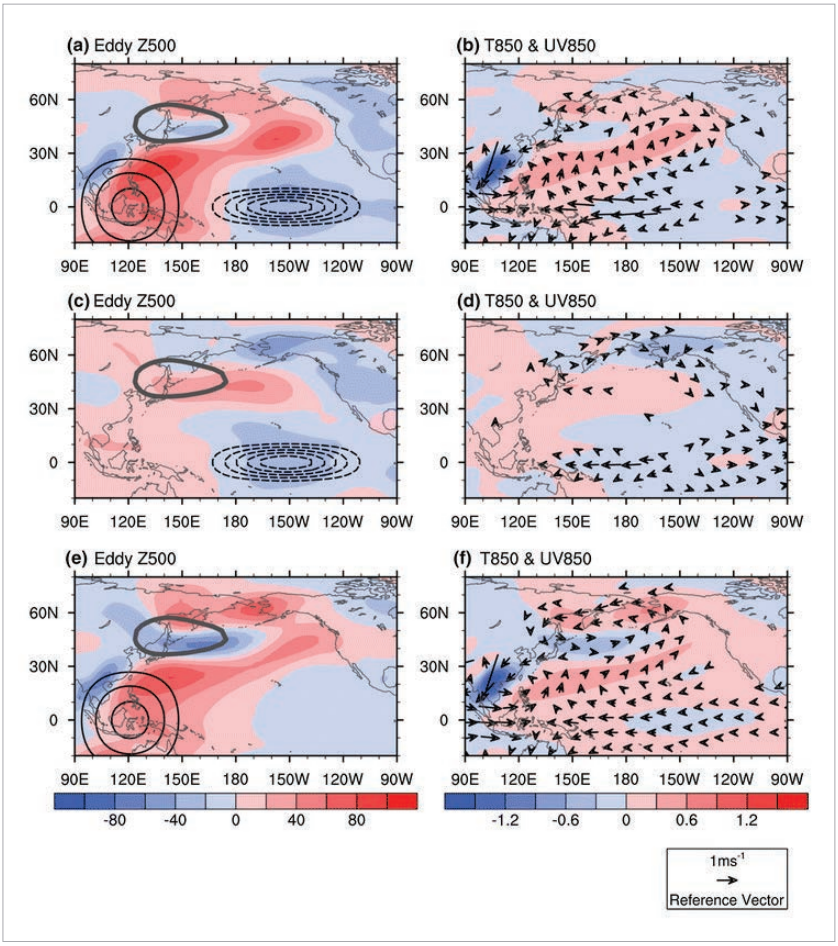

Figure 3. (a, c, e) 500-hPa height anomalies (shading; unit: m), (b, d, f) 850-hPa air temperature anomalies (shading; unit: K) and wind anomalies (vectors; only showing the magnitude > 0.04 m s^{-1}) in response to anomalous heat sources using a linearized AGCM prescribing the NDJ climatology. In (a, c, e), the solid (dashed) black contours represent heat sources (sinks) at the 0.5 sigma level with an interval of 0.2 K day^{-1}. The thick grey contours indicate the climatology of –150 m eddy height.

Reference:

Leung, Y. T., H. H. N. Cheung and W. Zhou, 2016: Meridional displacement of the East Asian trough and its response to ENSO forcing. *Climate Dynamics*, doi: 10.1007/s00382-016-3077-8.

A4. Synoptic-scale waves in sheared background flow over the western North Pacific

(PI: Wen ZHOU)

Results exhibit that different ambient sheared flows significantly affect the vertical structure of westward-propagating TD-type waves, with a lower-tropospheric mode in an easterly sheared background and an upper-tropospheric mode in a westerly sheared background (Figure 4). Energetic diagnoses demonstrate that when the disturbance is trapped in the lower (upper) level by easterly (westerly) shear, the horizontal mean flow in the lower (upper) level favors wave growth by converting energy from the shear of the zonal mean flow (from the convergence of the meridional mean flow). During the penetration of a westward-propagating synoptic-scale disturbance from a westerly sheared flow into an easterly sheared flow, the upper-level disturbance decays, and the lower-level disturbance intensifies. Meanwhile, the upper-level kinetic energy is transferred downward, but the effect induces the wave growth only confined to the mid levels. For more details, please refer to Feng et al. (2016).

This study reveals the characteristics and energetics of convectively coupled TD-type waves under the effects of different circulation patterns in association with vertical wind shear.

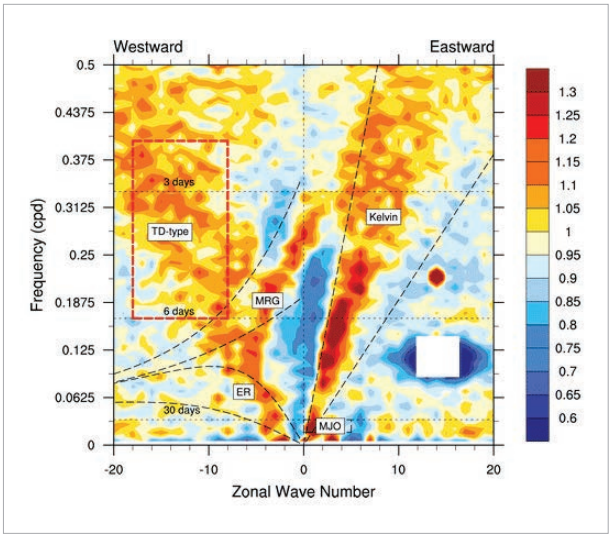

Figure 4. Wavenumber-frequency spectrum of the OLR over the Northern Hemisphere from June to November 1979–2013. The filter band for TD-type waves is indicated by the red dashed rectangle.

Reference:

Feng, T., X. Q. Yang, W. Zhou, R. H. Huang, L. Wu and D. J. Yang, 2016: Synoptic-scale waves in sheared background flow over the western North Pacific. *Journal of the Atmospheric Sciences*, 73, 4583-4603.

B. Precipitation Variability

B1. Understanding and detecting super-extreme droughts in southwest China through an integrated approach and index

(PI: Wen ZHOU)

In the last decade, a series of super-extreme droughts have swept across Southwest China (SWC) (Figure 5). However, the essential features behind them are not yet fully understood and traditional drought indices as well as precipitation fail to describe them due to the lack of a comprehensive treatment of drought. Re-examination of SWC droughts illuminates the essential feature of super-drought events: a combination of multiple stresses on water resources, which highlights the utility of the Comprehensive Multiscalar Indicator. For more details, please refer to Wang et al. (2016).

An integrated metric, the Comprehensive Multiscalar Indicator, was proposed as a new criterion for super-drought detection.

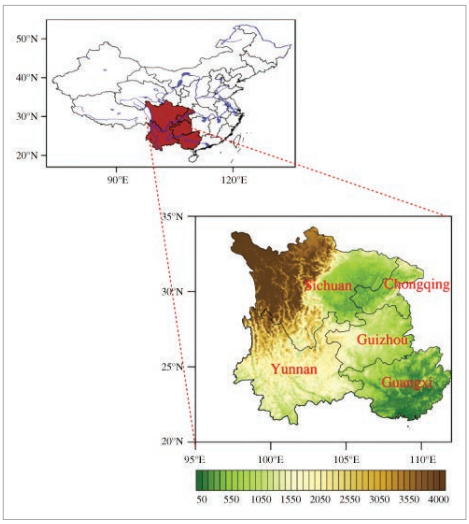

Figure 5. Location of Southwest China (top left) and its topography (bottom right, unit: m).

Reference:

Wang, L., W. Chen, W. Zhou and G. Huang, 2016: Understanding and detecting super-extreme droughts in Southwest China through an integrated approach and index. *Quarterly Journal of the Royal Meteorological Society*, 142, 529-535, doi: 10.1002/qj.2593.

B2. Detecting the origins of moisture over southeast China

(PI: Wen ZHOU)

The HYSPLIT model provides more insightful information than water vapor flux. Analysis of the specific humidity along the trajectories revealed the origins of moisture and their contributions to the moisture supply in Southeast China.

This study examines the ability of the Hybrid Single-Particle Lagrangian Integrated Trajectory (HYSPLIT) model to detect the origins and paths of moisture supplied to Southeast China, trajectories of air particles released over Southeast China were traced backward during 1 April 2012 to 31 March 2013 and three typical regional persistent heavy rainfall events. In the boreal summer half year, four key moisture transport paths from the eastern Indian Ocean, central Indian Ocean, South China Sea, and western North Pacific (WNP) contribute 10%, 20%, 31%, and 16% of the moisture to Southeast China, respectively. In the winter half year, the contributions of the paths from the WNP and North China double (Figure 6). For more details, please refer to Li et al. (2016).

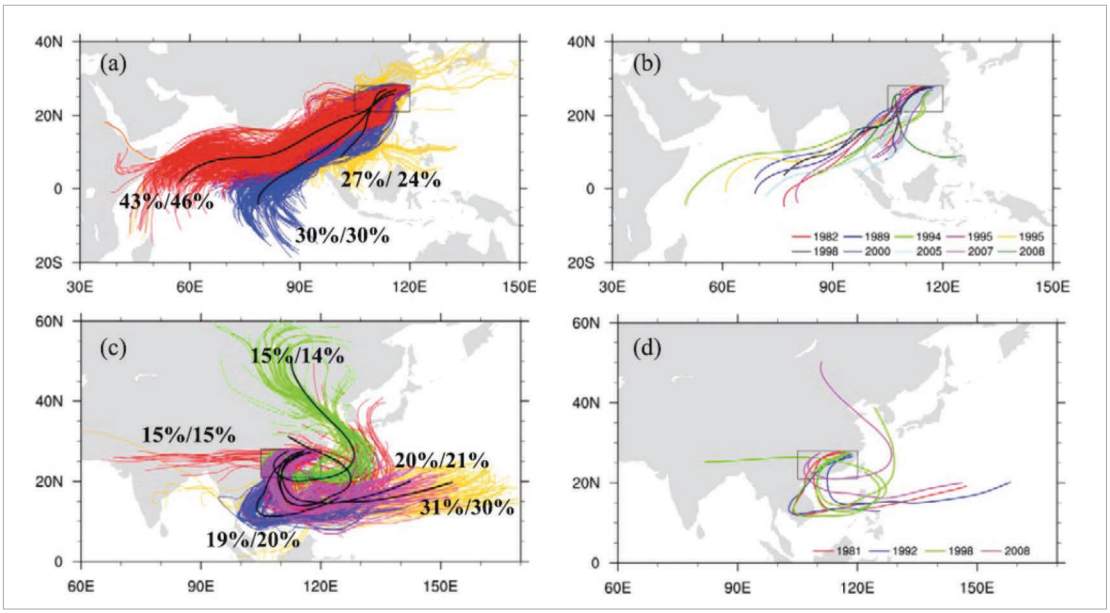

Figure 6. Cluster analysis of (a, b) type II interaction of the westward WPSH and cold air activity in the summer half year and (c, d) type III strong cold air activity in the winter half year. In (a, c) trajectories with different colours represent different clusters, and the black line represents the composited trajectory of each cluster; in (c, d) trajectories with different colours represent clustering results in each heavy rainfall case.

Reference:

Li, X. Z., W. Zhou and Y. Q. Chen, 2016: Detecting the origins of moisture over Southeast China: Seasonal variation and heavy rainfall. *Advances in Atmospheric Sciences*, 33, 319-329.

C. Tropical Cyclone

C1. Changing relationship between La Niña and tropical cyclone landfalling activity in South China

(PI: Johnny CHAN)

This study examines the effect of El Niño-Southern Oscillation and Indo-Pacific warm pool sea-surface temperature on tropical cyclone landfalling activity along the South China coast.

This study investigates the effect of El Niño-Southern Oscillation and Indo-Pacific warm pool sea-surface temperature (SST) on tropical cyclone (TC) landfalling activity along the South China coast and develops a scheme for predicting this activity. In general, landfalling activity tends to be suppressed in El Niño years but a large uncertainty is found for La Niña years (Figure 7). Landfalling activity is generally enhanced in La Niña years before 1997 but suppressed in those after 1997, which may be related to the changes in overall TC activity and track pattern over the western North Pacific (WNP) as well as the northward shift in genesis locations. The Indo-Pacific warm pool SST is found to be related to the TC activity over the WNP and an SST index, defined as the average SST anomalies over the North Indian Ocean and the sea near the Philippines, is used to represent this anomaly. A significant warming of the Indo-Pacific warm pool is found in the recent decade and its SST change appears to modulate the TC activity over the WNP and TC landfalling activity in South China in a La Niña year, with an enhancement (a suppression) of TC activity if a cooling (warming) is found. This difference is shown to be related to the changes in the strength of monsoon trough, vertical wind shear and steering flow pattern. Based on these results, a schematic prediction scheme of landfalling activity in South China is proposed (Figure 8). Landfalling activity is likely to be normal or below normal if an El Niño event is expected to develop during the TC season. If a La Niña event is expected, and the predicted state of the Indo-Pacific warm pool (obtained using the persistence forecast) shows a warming (cooling), landfalling activity is likely to be normal or below normal (above normal). For more details, please refer to Liu and Chan (2017).

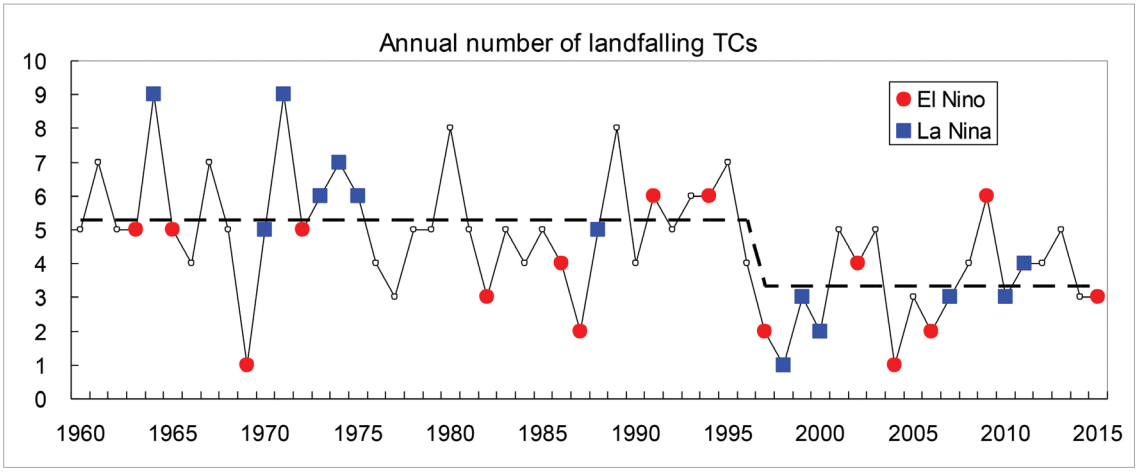

Figure 7. Time series of the annual number of landfalling TCs in South China. Red closed circles and blue closed squares denote the El Niño and La Niña years respectively. The dashed lines indicate the regime shifts.

Figure 8. The schematic prediction scheme of the seasonal forecast of the annual number of TCs making landfall in South China.

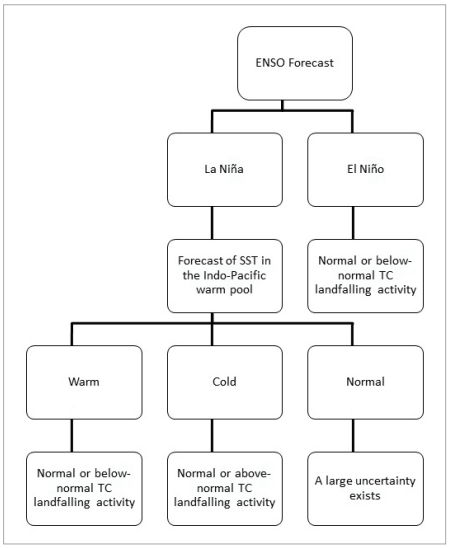

Reference:

Liu, K. S. and J. C. L. Chan, 2017: Changing relationship between La Niña and tropical cyclone landfalling activity in South China. Submitted to *International Journal of Climatology*.

C2. Simulating seasonal tropical cyclone intensities at landfall

(PI: Johnny CHAN)

This study examines the RegCM-WRF model system in predicting tropical cyclone intensity at landfall on a seasonal basis.

Based on the dynamical downscaling model developed by Huang and Chan (2014), a mesoscale model (WRF) is further nested on the regional climate model (RegCM) to downscale tropical cyclone (TC) intensity at landfall. The model system is driven from the NCEP CFSR dataset, and it is validated against the JTWC best tracks. Results show that the model system can produce a reasonable distribution of TC intensity at landfall on a seasonal scale in the South China region (Figure 9) and has a better skill in predicting TC landfall intensity than a global model alone. This study shows that the subtropical ridge in the East China Sea is crucial to predicting TC landfall in the South China. If the ridge is stronger over the course of the season, more intense tropical cyclones will make landfall in Guangdong and Hainan provinces (Figure 10), and vice versa. This study demonstrates the potential of the model system in seasonal prediction as well as climate projection. For more details, please refer to Lok and Chan (2017).

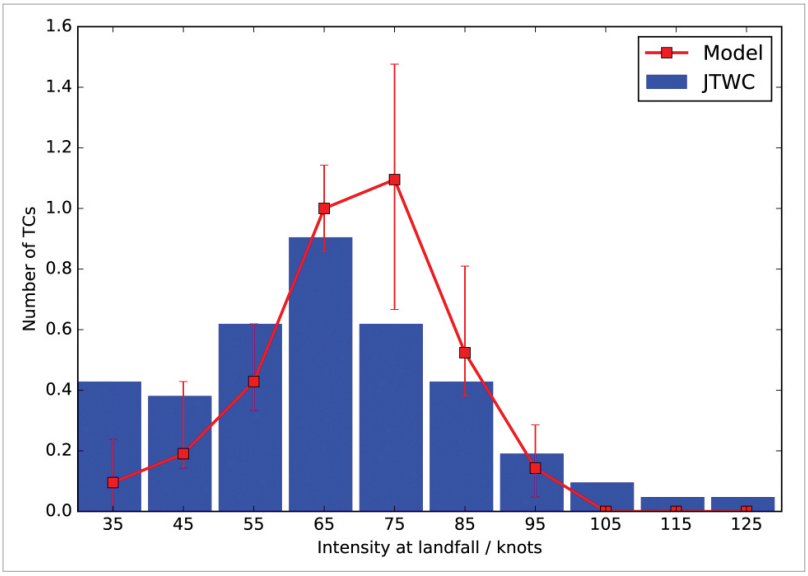

Figure 9. Intensity distribution of the TCs making landfall in South China from 1990 to 2010. Blue bars are the JTWC data. Squared red line plots the model result with whiskers showing the ensemble spreads. TC intensities are grouped every 10 knots, and the median values are shown. The distribution excludes TCs with maximum sustained winds less than 30 knots.

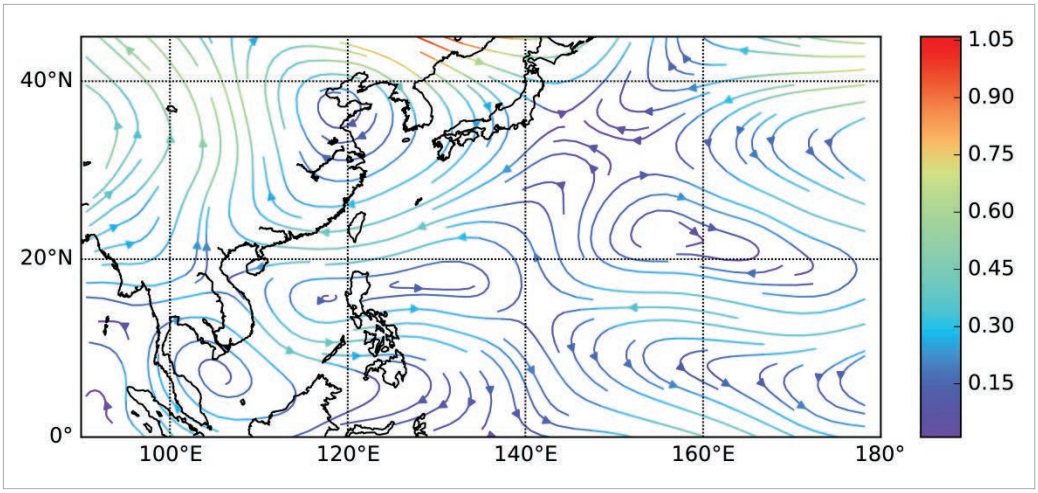

Figure 10. RegCM3 850-300 hPa layer-mean flow pattern anomalies of the top 25% annual TC landfalls in South China. Units of the colour bar is m/s.

Reference:

Huang, W. R. and J. C. L. Chan, 2014: Dynamical downscaling forecasts of western North Pacific tropical cyclone genesis and landfall. *Climate Dynamics*, 42, 2227-2237.

Lok, C. C. F. and J. C. L. Chan, 2017: Simulating seasonal tropical cyclone intensities at landfall along the South China coast. Submitted to *Climate Dynamics*.

D. Effect of Urbanization

D1. Sensitivity of precipitation statistics to urban growth in a subtropical coastal megacity cluster

(PI: Johnny CHAN)

This study examines the effect of cities with different sizes on local precipitation microclimate.

In this study, we investigate the question, whether or not cities of significantly large and small sizes affect the local precipitation microclimate within their boundaries and region. A benchmark monsoon trough case in the time period from 5 to 8 June 2008 is studied in the Pearl River Delta region for two different sets of land use conditions, a reasonably modern dataset with one in which the urban area is represented as it was approximately 20 years earlier. Additionally different degrees of human activity have been studied by varying the anthropogenic heat flux parameter. The two different stages of urban development show significant differences in their effects on precipitation statistics. The modern and large city produces more heavy local rainfall through production of buoyancy and hence triggering of convection, while the old and smaller urban area does not introduce sufficient buoyancy to introduce local convergence and trigger convection locally, but remotely through advection processes (Figure 11). The full description of the research is available in the article by Holst et al. (2017).

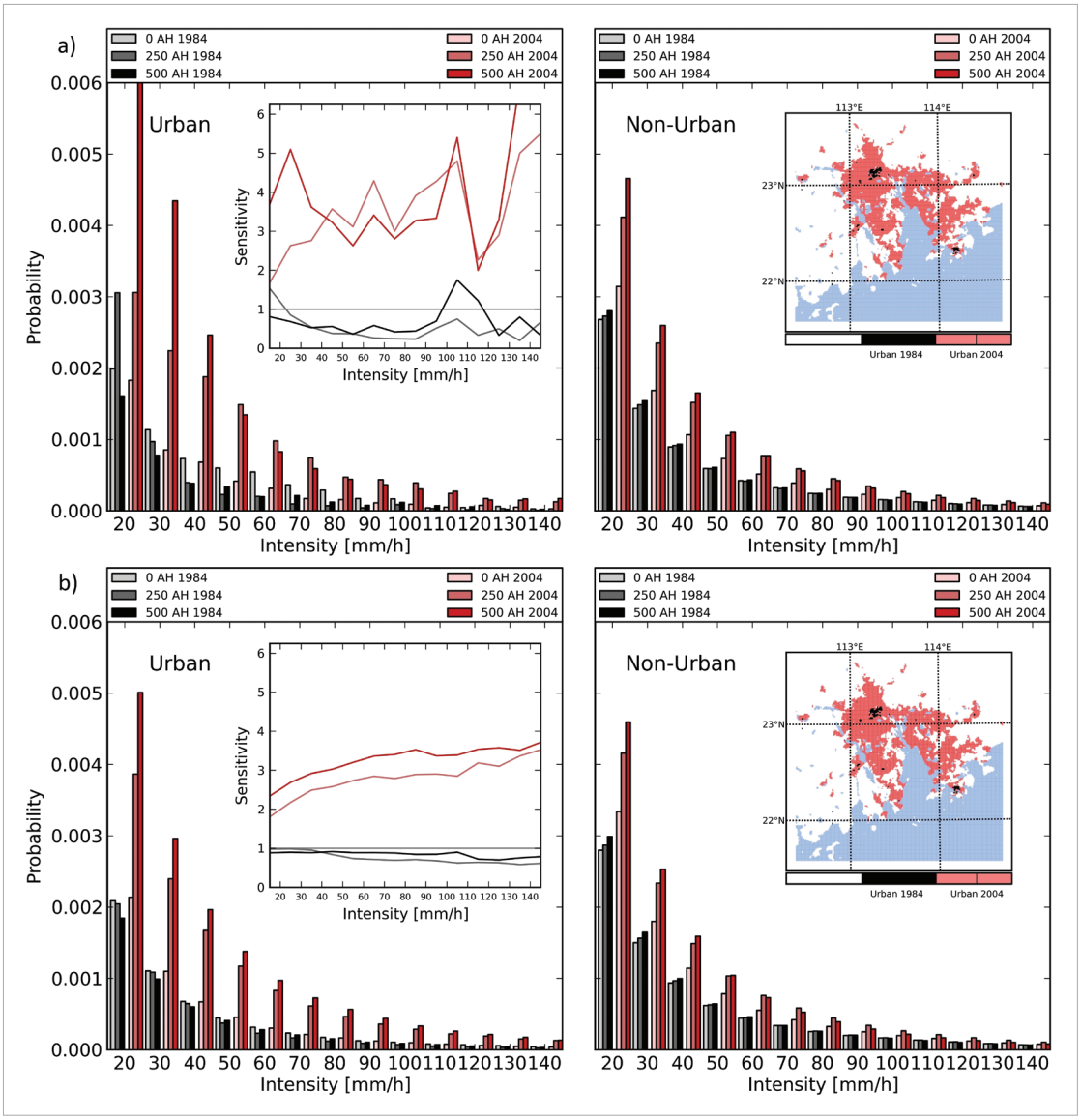

Figure 11. Probability density functions for different 5 minute interval hourly precipitation rate bands as shown on the horizontal axis. The black bars refer to small city's forcing effects while the red bars refer to the large city's effects. The magnitude of the surface heat flux scales from 0 (pale colours) to the maximum amplitude of 500 Wm^{-2} (full colours). The left and right panels of the figure show urban and non-urban behaviour respectively. The sampling was carried out as shown in the right insets for the (a) small (black) and (b) large city extend (red area). The left insets show the different sensitivity of the precipitation to human activities as induced by anthropogenic heat flux.

Reference:

Holst, C. C., J. C. L. Chan and C. Y. Tam, 2017: Sensitivity of precipitation statistics to urban growth in a subtropical coastal megacity cluster. *Journal of Environmental Sciences*, doi: 10.1016/j.jes.2017.01.004.

E. Air Quality

E1. Correction algorithm development and error analysis of electrochemical sensors for ambient air quality monitoring

(PI: Zhi NING)

Correction algorithms for next generation air sensors are developed and evaluated.

The increasing demand for use of low-cost air sensors promises more convenient and cost-effective systems for air monitoring in many places and conditions. However, the data quality from such systems has not been fully characterized and they may not meet research or regulatory user expectations. In our study, electrochemical sensors (Alfasense B4 series) for carbon monoxide (CO), nitric oxide (NO), nitrogen dioxide (NO_2) and ozone (O_3) were evaluated under controlled laboratory conditions to identify factors and quantify their relation with sensor outputs. Based on the laboratory tests, we developed different correction algorithms to compensate the impact of ambient conditions. Further, the sensors were also tested in field ambient conditions of Hong Kong side by side to the regulatory reference monitors, and the data from these tests were used to evaluate the performance of the models and validate their applicability in different ambient conditions. The more comprehensive correction models demonstrated enhanced performance when compared with uncorrected data. One over-arching observation of this study is that the low-cost sensors may promise excellent sensitivity and performance, but it is essential for users to understand and account for key factors that may strongly impact the nature of sensor data.

The laboratory tests were conducted to establish the relation of output from the electrochemical sensors with concentration of individual gases (NO_2, NO, O_3, CO) and controlled laboratory conditions. Different models of commonly used electrochemical sensors including NO_2-B42F (NO_2), NO-B4 (NO), CO-B4 (CO), and OX-B421 (combined oxidant gases NO_2 and O_3) (Alphasense, UK) were tested to evaluate the sensor linearity, impact of temperature and humidity, cross interference and long term drift. The test setup is composed of 4 major components as shown in Figure 12. Figure 13 shows the time series of ambient conditions during the field test carried out in the urban site. There was a large variation of the relative humidity (54% to 95%) and mild range of temperature (17 to 24 °C) during the period, which produced a good opportunity for the evaluation of different models. Figure 14 further illustrates the box plots of error distribution for all the models using data from validation period. The solid round dots and rectangular dots represent 1% and 99% percentile, and mean value respectively. The 4 inflection points of the box margin from the bottom to top represent 10%, 25%, 75%, and 90% percentile of the errors, and the bar in the middle of the box is the median value. Figure 15 presents the histogram of the errors from Model 0 without correction and optimal model chosen from regression analysis. The errors are calculated from the 5 min resolution AQMS and sensor data, and they follow closely a normal distribution with mean value around 0 and long tails along both sides. The red and black lines are the fitted normal distribution curves for Model 0 and optimal model, respectively. The errors from optimal model clearly had a narrower distribution. F-test were performed for all the four sets of sensor data and there was a significant difference between the variation of error from Model 0 and optimal model ($p < 0.001$) at a significance level of 0.05, demonstrating the improvement of measurement precision using the optimal model. Using 1 standard deviation of the error distribution as an indicator, the CO, NO, NO_2 and O_x sensors showed an improvement of 41% from 8.3 to 5.9 ppb, 35% from 0.05 to 0.03 ppm, 22% from 7.4 to 6.1 ppb, and 32% from 7.4 to 5.6 ppb, respectively.

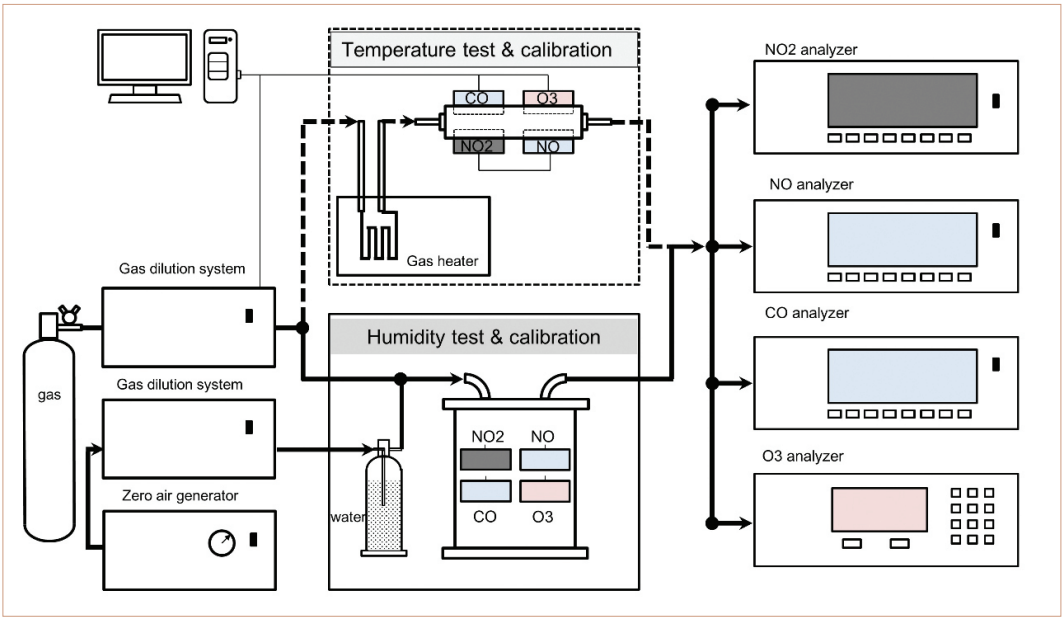

Figure 12. Laboratory setup for sensor linearity, cross sensitivity and zero air drift test.

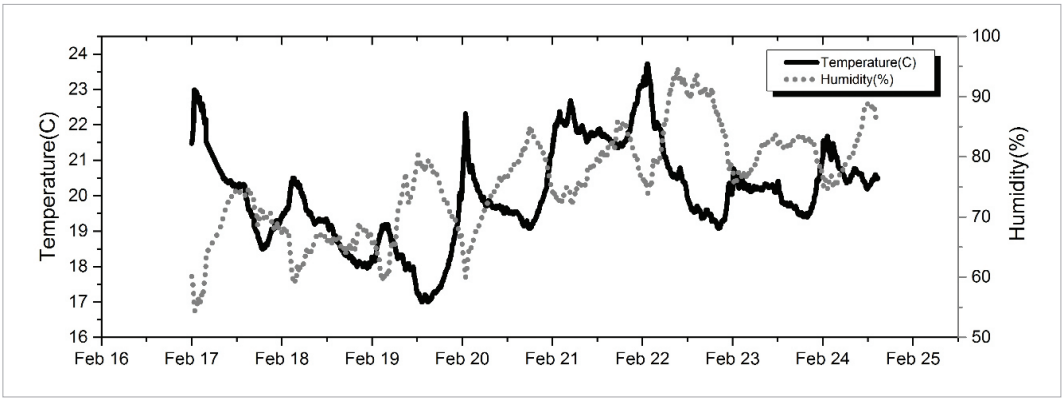

Figure 13. The ambient temperature and relative humidity during field test.

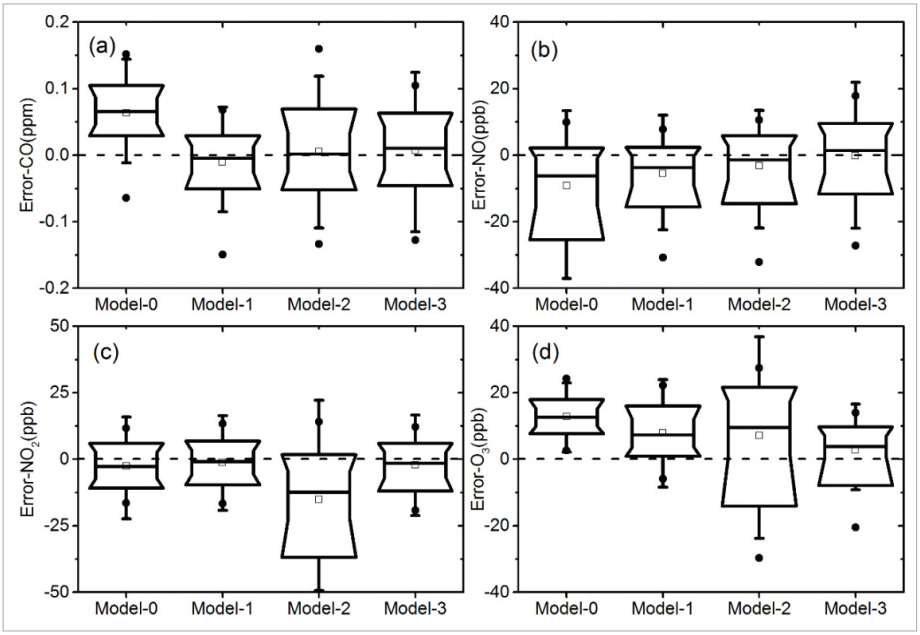

Figure 14. Box plots of error distribution of 4 models (a) CO, (b) NO, (c) NO_2 and (d) O_3.

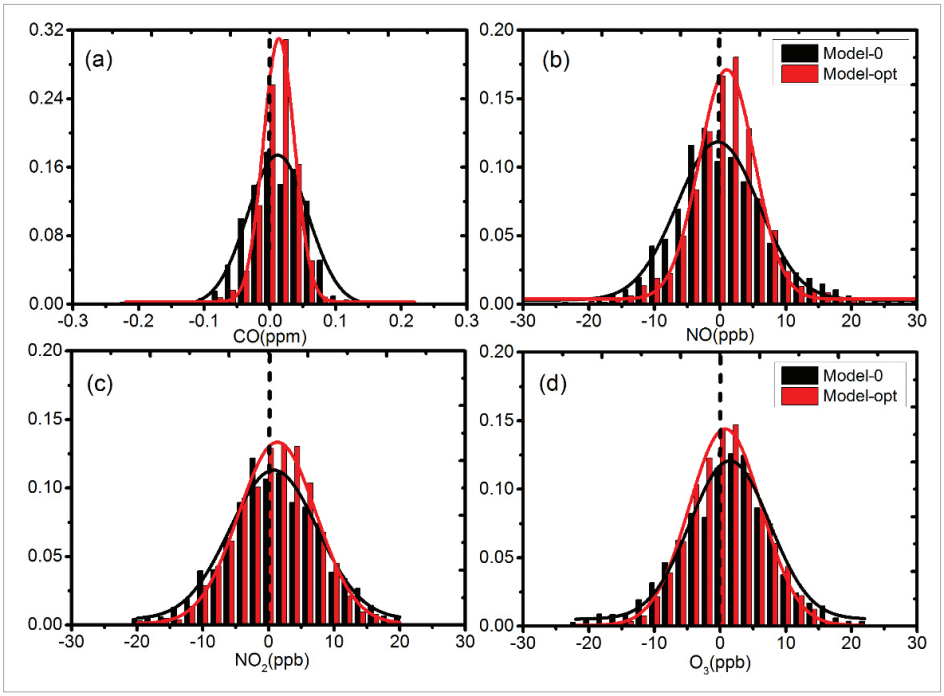

Figure 15. Histogram of errors from models fitted with normal distribution curves (a) CO, (b) NO, (c) NO_2 and (d) O_3.

Reference:

Wei, P., Z. Ning, S. Ye, L. Sun, F. Yang, K. C. Wong, D. Westerdahl and P. Louie, 2016: Correction algorithm development and error analysis of electrochemical sensors for ambient air quality monitoring. Submitted to *Sensors*.

E2. Investigation on the mechanism of non-photocatalytically TiO_2-induced reactive oxygen species and its significance on cell cycle and morphology

(PI: Zhi NING)

Nanoparticle toxicity is investigated with understanding of the mechanism in health effect.

Titanium dioxide (TiO_2) nanoparticles are widely used in daily human life, and were reported to elicit biological effects such as oxidative stress either generating reactive oxygen species (ROS) or causing cell necrosis without generating ROS, whose underlying molecular mechanisms are not yet known. In this study, the role of dissolved oxygen in TiO_2 catalytic activity in dark environment, and long-term cytotoxic effects of TiO_2 exposure were investigated. To determine the effect of dissolved oxygen, the anatase-TiO_2 nanoparticle suspension was prepared both in deoxygenated and regular MilliQ water, and a ~ 9-fold higher ROS in regular MilliQ samples was observed compared to deoxygenated samples while in the dark, which suggested dissolved oxygen as the driving agent behind the TiO_2 catalytic reaction. On the other hand, the differential cell viability and endogenous ROS activity was demonstrated through a sensitive macrophage-based assay, on a dose- and time-dependent manner. Both the cell number and endogenous ROS activity increased with increase in time till 48 h, followed by a reduction at 72 h exposure period. Long-term exposures to these nanoparticles even at low concentrations were found detrimental to cells, where late apoptosis until 48 h and necrosis at 72 h leading to cell death were noted. Late apoptotic events and cell membrane cytoskeletal actin rearrangement observed were hypothesized to be induced by particle-mediated cellular ROS. This in addition to radical generation ability of TiO_2 in the dark will help further in better understanding of the toxicity mechanism in cells beyond ROS generation.

Figure 16 shows the effect of nanoparticle suspension on macrophage viability at different time intervals and concentrations. The cell viability of nanoparticle treated samples remained unchanged until four hour exposure (data

not shown), while an increase in viability was observed for 24 and 48 h exposure (with 0.01 µg/ml) by 20% (p=0.011, N=3) and 60% (p<0.001, N=3) respectively, compared to untreated cells (not shown in figure, as untreated cell controls remained viable in the range 98-100% for all time intervals). Extended 72 h exposure, however, resulted in a reduction of cell viability by 15% (p=0.017, N=3), whereas, other two concentrations (0.10 and 1.00 µg/ml) decreased cell viability by 5 to 15 % for 24 and 48 h, and 25% at the end of 72 h.

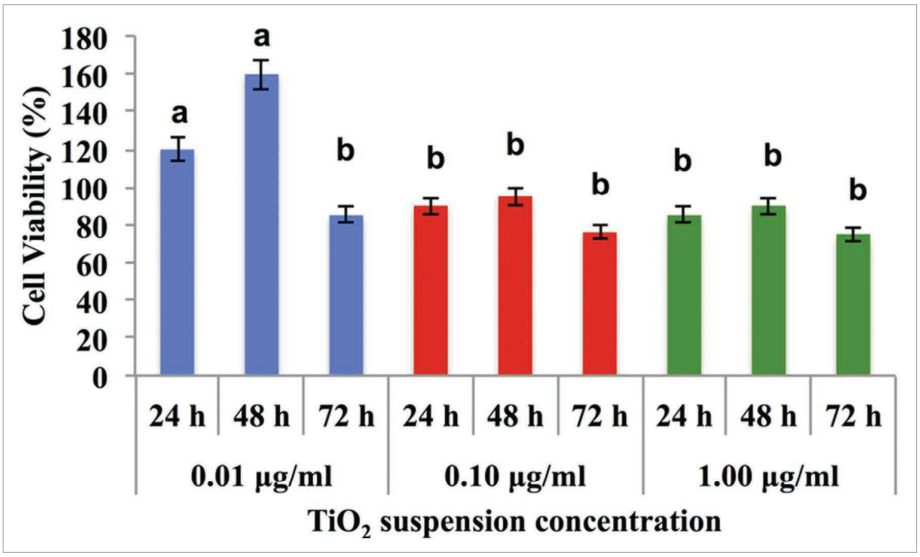

Figure 16. Comparative analysis of cell viability.

Reference:

Gali, N. K., Z. Ning, W. Daoud and P. Brimblecombe, 2016: Investigation on the mechanism of non-photocatalytically TiO_2-induced reactive oxygen species and its significance on cell cycle and morphology. *Journal of Applied Toxicology*, doi: 10.1002/jat.3341.

E3. Implication of light absorption enhancement and mixing state of black carbon by coatings in urban aerosol

(PI: Zhi NING)

Light absorption enhancement and mixing state of black carbon are evaluated by coatings in urban aerosol.

Simultaneous measurement of black carbon (BC) and other aerosol chemical compositions was performed using an Aethalometer (AE33) and Aerosol Chemical Speciation Monitor (ACSM) in urban area of Hong Kong. A thermodenuder (TD) was employed in tandem with AE33 and ACSM at different heating temperatures (i.e., 50°C, 100°C, 150°C, 200°C and 280°C) to remove semi-volatile aerosol fractions (i.e., coatings) by different degree. By comparing the measurements of non-heated and heated aerosol, we evaluated light absorption enhancement (E_{abs}) of BC by coatings in seven wavelengths from UV to near IR region, and further analysed the aerosol coating compositions. Result showed E_{abs} increased very little from 50°C (1.02 – 1.04) to 200°C (1.13 – 1.20), but surged to 1.58 (470nm) – 1.64 (660nm) at 280°C, probably attributed to the presence of low volatility inorganic components such as ammonium and sulfate, which might be associated to lensing effect. The absorption Angström exponent (AAE) had slight increase after heating, possibly due to higher light absorption for low-volatility brown carbon (BrC_{LV}) at UV wavelength region, as also indicated by inverse Mie calculation that imaginary part *k* of BrC_{LV} could be as high as 0.02 ~ 0.15. Furthermore, the ratio of coating thickness to BC core radius was around 100% ~ 200% based on Mie calculation. This work showed the impact of source- and region- based difference on E_{abs} and could provide critical reference for climate model on the role of aerosol in global warming.

The design of the thermal denuder is shown in Figure 17. Figure 18 showed the comparison of temperature profile measured from the TD at a fixed temperature of 280°C referred in others and our study. Our TD is comparable to Wehner TD, though the inlet temperature of our TD is a little lower. Both Wehner TD and our TD have high exit temperature, which would avoid recondensation before evaporated gases were adsorbed by activated charcoal.

TD losses are inevitable due to sedimentation, diffusion and thermophoresis inside the heating tube. In this work, we use elemental carbon (EC) which is refractory at high temperature to quantify the temperature-dependent TD loss at different temperature (i.e., 25°C, 100°C, 150°C, 200°C, 280°C), by collecting filter samples through TD and non-TD lines with two cascade $PM_{2.5}$ impactors. EC was then measured with an OCEC analyser (Sunset Laboratory Inc.), following the NIOSH 5040 protocol (Birch and Cary, 1996). A transmission efficiency equation as a function of temperature $\eta_t = 1.0111 - 0.0003*T$ ($R = -0.79$, $p < 0.01$) was then determined, in which η_t is transmission efficiency and T is the set temperature in Celsius (°C). All calculations below were corrected by applying this transmission efficiency. Without this correction, E_{abs} will be overestimated.

AAE derived from aerosol passing through TD are a little higher than that from ambient aerosol without TD as shown in Figure 19, which is mathematically attributed to a slightly smaller decrease rate of b_{abs} at short wavelength than that at long wavelength after heating. For example, a decrease of ~ 41% in b_{abs} was observed at 660nm – 950nm after heating at 280°C compared to ~ 39% at 370nm – 470nm, indicating the existence of a stronger absorption of low volatile organics which were still present after 280°C heating. In contrast to our result, Devi et al., (2016) observed an average AAE of 1.4 before heating at 200°C and 1.1 after heating in urban Atlanta, while at rural Centerville it didn't show any major change with AAE value of 0.99 and 0.98. The resultant discrepancy may probably be attributed to source specific differences of aerosol chemical composition, since AAE of our observation on ambient aerosol was only around 1.1 – 1.2. Figure 20 is the result from the Mie calculation assuming 20% of coating materials remained, $E_{abs\text{-}Mie}$ increased with increasing coating fraction (f_{coat}), from 1.3 to as high as ~ 2.8 (370nm), though in most cases $E_{abs\text{-}Mie}$ mainly distributed in 1.5 ~ 1.7 (refer to the green area), with coating fraction mainly from 100% to 200%. $E_{abs\text{-}Mie}$ also decreased from UV to IR wavelength, which could be attributed to the absence of UV-absorbing BrC. Figure 20b displayed the varied E_{abs} with increased imaginary part k for low-volatile coatings at 370nm. In order to achieve an E_{abs} of ~ 1.6 at 370nm based on our observation with coating fraction ranged from 100% to 200%, the imaginary k of low-volatile coatings is possibly distributed around 0.02 ~ 0.15 (see the green area), which is much higher than assumed k of 0.006, indicating much higher absorption ability for BrC_{LV}.

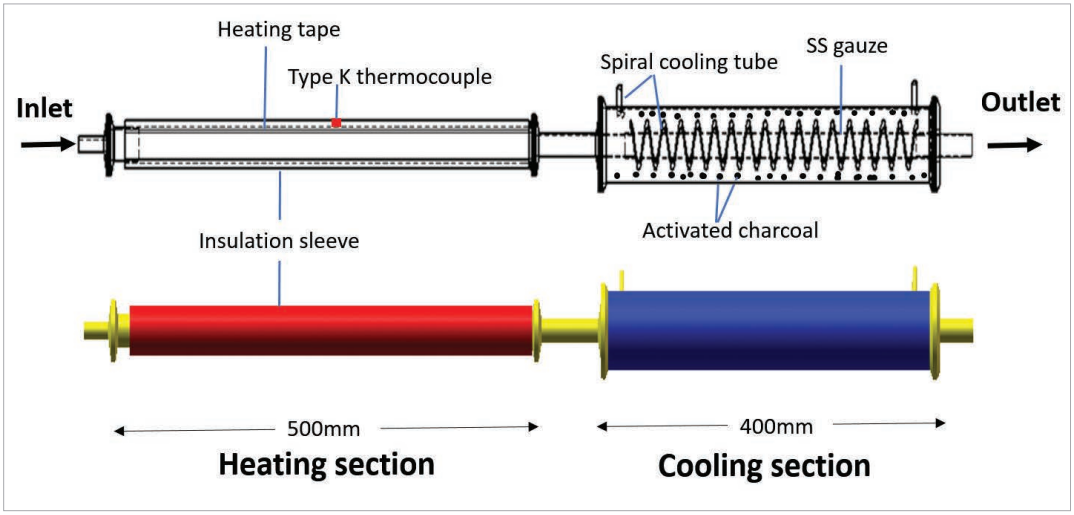

Figure 17. Design schematic of the thermodenuder.

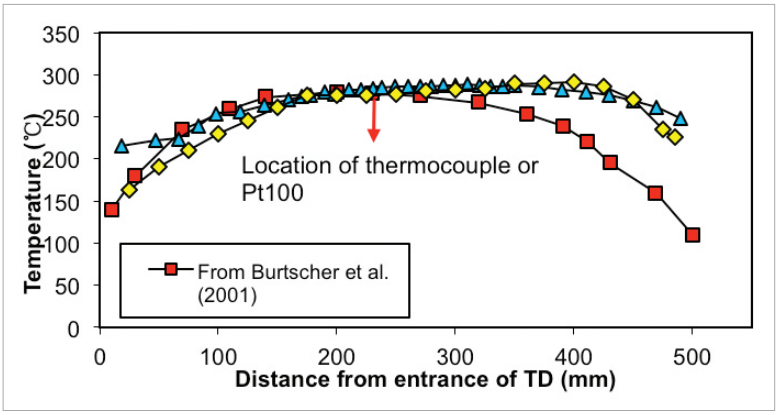

Figure 18. Comparison of temperature profile inside the heating tube at a fixed temperature of 280°C.

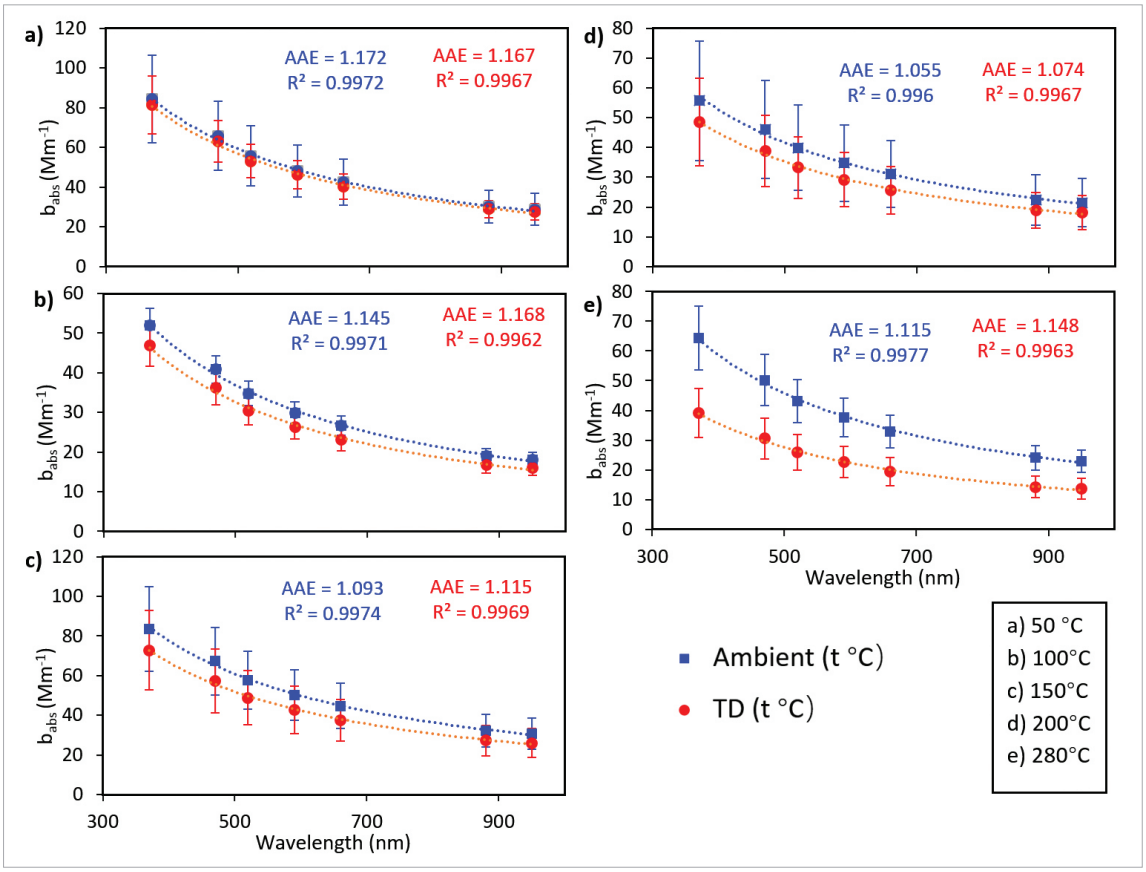

Figure 19. Light absorption coefficient (b_{abs}) of heated (T temperature) and corresponding ambient aerosol and fitted AAE.

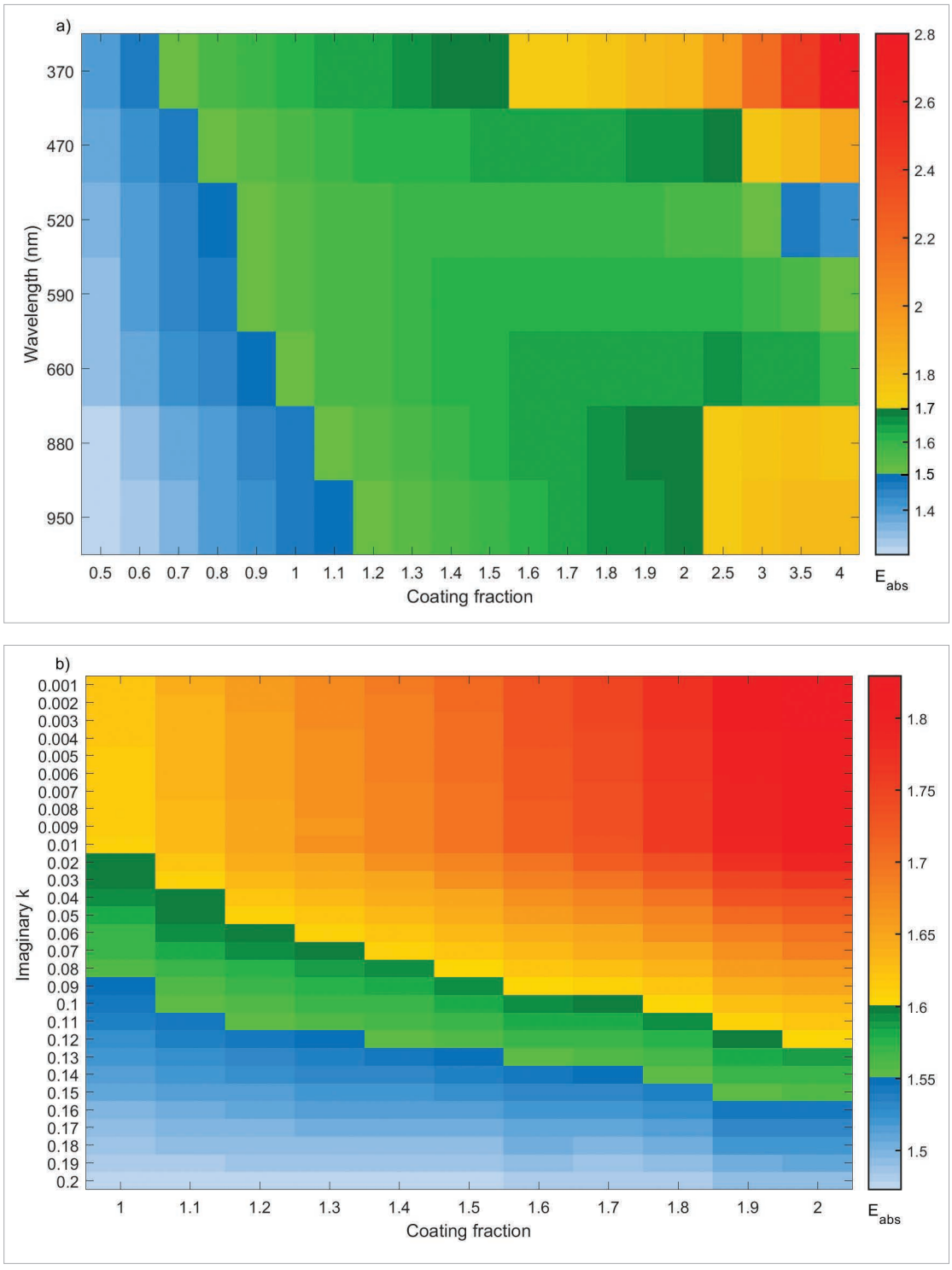

Figure 20. Assuming 20% coatings remained, a) E_{abs} calculated by Mie theory based on different coating fraction. b) E_{abs} varied with increased imaginary part k for low-volatile coatings at 370nm, with coating fraction from 100% to 200%. Note that E_{abs} included the absorption contribution of BrC. Green zone was targeted area for Mie calculation in well agreement with field measurement.

Reference:

Li, G., J. Zhang, K. F. Ho, Z. Ning and K. C. Wong, 2016: Implication of light absorption enhancement and mixing state of black carbon by coatings in urban aerosol. Submitted to *Environmental Science and Technology*.

E4. Study of traffic-related pollutant removal from street canyon with trees: dispersion and deposition perspective

(PI: Nicky LAM)

This study applied a computational fluid dynamics model, ENVI-met, to investigate the removal ability of trees on $PM_{2.5}$.

In this study, a computational fluid dynamics (CFD) model, ENVI-met, was used to investigate the removal ability of trees on $PM_{2.5}$ based on the effects of dispersion and tree deposition. Several parameters including the aspect ratio of buildings, tree planting patterns, the leaf area index/density distribution, the trunk height and the tree-covered area were examined (see Figure 21 for the schematic view of the experiment). Our results show that the concentration level of $PM_{2.5}$ is getting higher at the pedestrian walk inside the street canyons when trees were planted in most of the cases. Although $PM_{2.5}$ deposition on tree leaves has an effect on overall $PM_{2.5}$, the effect has been reduced due to the counter effect of lower dispersion. This study shows that careful tree planting is important in order to maximize the removal ability of trees on $PM_{2.5}$. For more information, please refer to Morakinyo and Lam (2016).

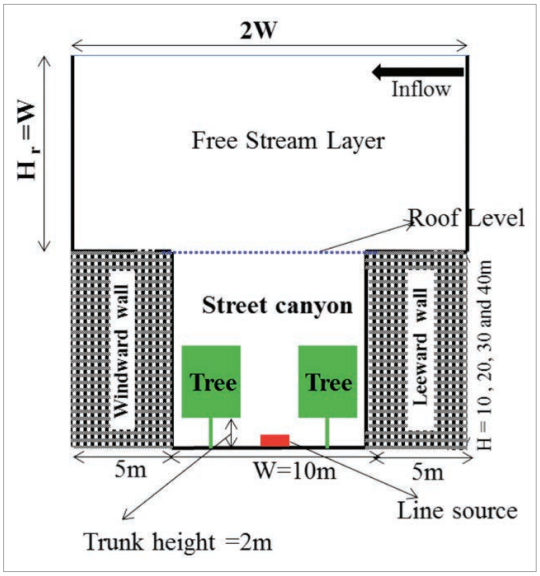

Figure 21. Schematic diagram of base cases for the trees and the street canyon.

Reference:

Morakinyo, T. E. and Y. F. Lam, 2016: Study of traffic-related pollutant removal from street canyon with trees: dispersion and deposition perspective. *Environmental Science and Pollution Research*, **23**, doi: 10.1007/s11356-016-7322-9.

E5. Impacts of southeast biomass burning on Hong Kong air quality

(PI: Nicky LAM)

This study investigates the air quality impacts of southeast biomass burning and its associated transport mechanism to Hong Kong.

In this study, HYSPLIT trajectory model coupled with Global Fire Emissions Database (GFED) and NCEP FNL (Final) Operational Global Analysis data was applied to investigate the effect of Southeast biomass burning (SEA-BB) on local air quality in the spring. An integrated approach was adopted to quantify both background and event-base air pollution enhancements from SEA-BB using 3 years' air quality observation (2012 to 2015). From our analysis, we found that, during 30 to 70% of the time (on a monthly

basis), SEA-BB was transported to the lower free troposphere of Hong Kong, while in only less than 15% of the time tropospheric downwash of SEA-BB occurred (Figure 22). In terms of air quality, the average background enhancement of CO, O_3, PM_{10} and $PM_{2.5}$ is found to be 113 μg/m^3, 2.3 μg/m^3, 5.6 μg/m^3 and 4.0 μg/m^3, respectively, while the maximum surface impacts during SEA-BB event could rise up to 184 μg/m^3, 17.6 μg/m^3, 22.5 μg/m^3, and 11.0 μg/m^3, respectively.

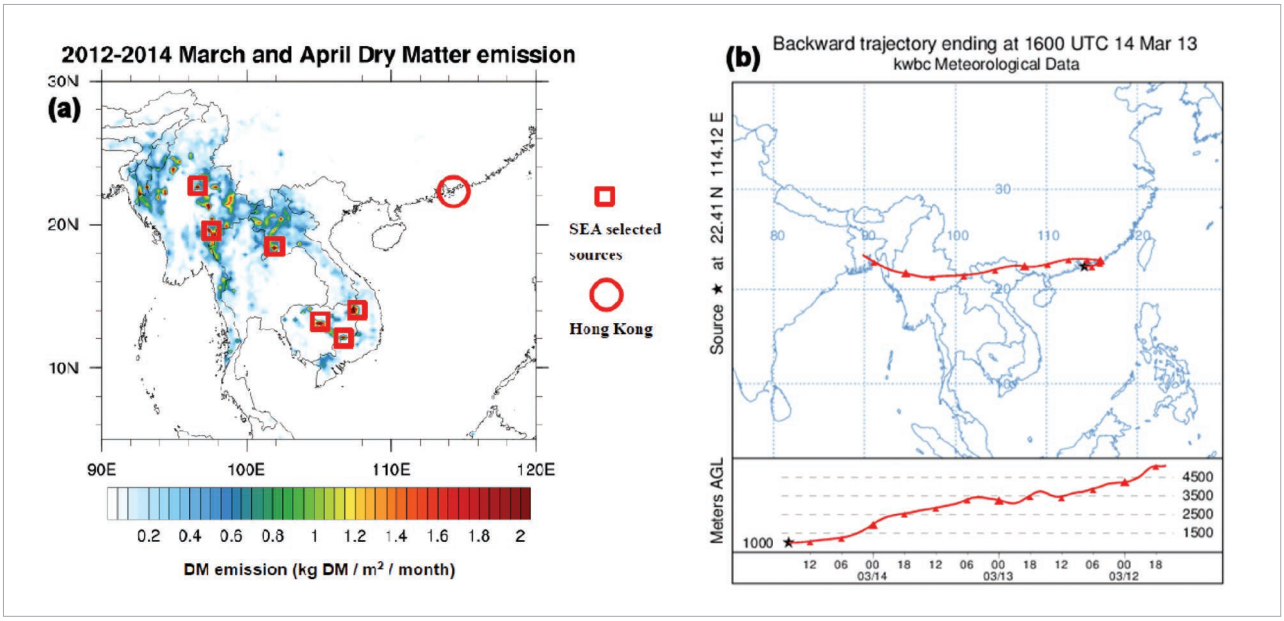

Figure 22. a. Selected source regions from GFED database for HYSPLIT trajectory modeling and b. Sample of backward trajectory that identified air pollution impacts on Hong Kong.

E6. Big traffic data applications: mobile emission estimates using GPS data

(PI: Nicky LAM)

This study utilizes local GPS data from onboard bus samplers to develop mobile emissions inventory for Hong Kong.

In this study, a new method was developed based on detailed position data collected from GPS/AGPS systems for mobile emission estimates. Samples were collected in the summer of 2015 for the Shatin district. It includes the occupancy rate, bus position, and elevation data. These data were then processed in ArcGIS to derive average travel speeds in the street level, and per bus-stop idling time for calculating segment-based emissions. Figure 23 shows the summary data collected in this study. Among all samples, 73% were collected during rush hours with average speeds of 20 km/hr and 50 km/hr for major arteries and highways, respectively. These low traffic speeds are found to be one of the major causes of roadside pollution in Hong Kong, as emission factors (NO_x and PM) at low speed are much larger than those at high speed (below 100 km/hr). Driving at low speed would result in more emissions on the street for the same vehicle. Therefore, this study suggests that increasing the average traffic speeds during rush hours would have a positive influence on total bus emissions.

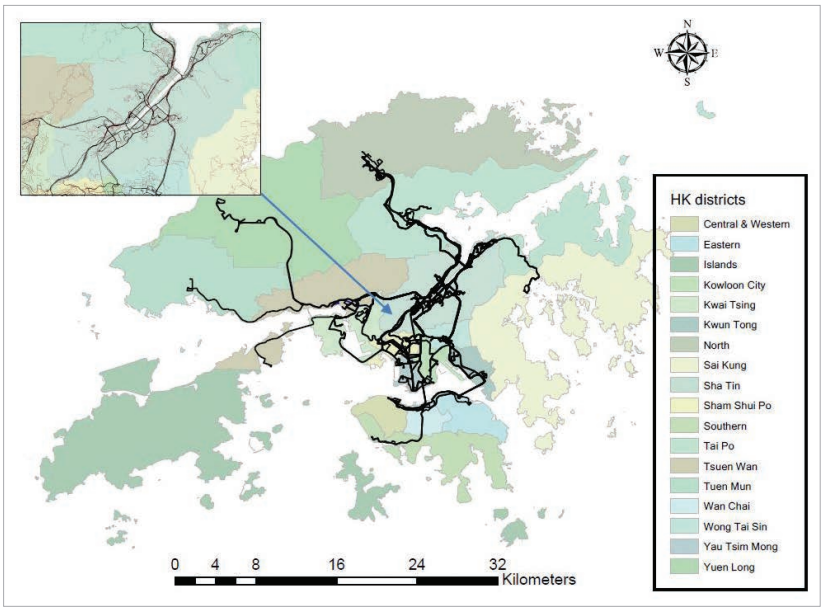

Figure 23. Sampling routes for all buses in and out Shatin district.

Publications

Journal Papers

Chan, K. L., S. Y. N. Jiang and Z. Ning, 2016: Speciation of water soluble iron in size segregated airborne particulate matter using LED based liquid waveguide with a novel dispersive absorption spectroscopic measurement technique. *Analytica Chimica Acta*, **914**, 100-109.

Cheung, H. H. N. and W. Zhou, 2016: Simple metrics for representing East Asian winter monsoon variability: Urals blocking and western Pacific teleconnection patterns. *Adv. Atmos. Sci.*, **33**, 695-705, doi: 10.1007/s00376-015-5204-6.

Cheung, H. H. N., W. Zhou, Y. T. Leung, C. M. Shun, S. M. Lee and H. W. Tong, 2016: A strong phase reversal of the Arctic Oscillation in midwinter 2015/16: Role of the stratospheric polar vortex and tropospheric blocking. *J. Geophys. Res. Atmos.*, doi: 10.1002/2016JD025288.

Feng, T., X. Q. Yang, W. Zhou, R. H. Huang, L. Wu and D. J. Yang, 2016: Synoptic-scale waves in sheared background flow over the western North Pacific. *J. Atmos. Sci.*, **73**, 4583-4603.

Holst, C., F. C. Y. Tam and J. C. L. Chan, 2016: Sensitivity of urban rainfall to anthropogenic heat flux - a numerical experiment. *Geophys. Res. Lett.*, **43**, 2240–2248, doi:10.1002/2015GL067628.

Hunt, J. C. R., J. C. L. Chan and J.-P. Wu, 2016: Asian urban environment and climate change. *Current Science*, **110**, 1398–1400.

Kaul, D. S., Z. Ning, D. Westerdahl, X. Yin and R. A. Cary, 2016: A novel tandem of thermal desorption carbon analyzer and off-axis integrated cavity output spectroscopy for aerosol stable carbon isotope ratio measurement. *Aerosol and Air Quality Research*, **16**, 1345-1355, doi: 10.4209/aaqr.2015.05.0288.

Kwok, L. K., Y. F. Lam and C.-Y. Tam, 2016: Developing a statistical based approach for predicting local air quality in complex terrain area. *Atmospheric Pollution Research*, **8**, 114-126, doi: 10.1016/j.apr.2016.08.001.

Leung, Y. T., H. H. N. Cheung and W. Zhou, 2016: Meridional displacement of the East Asian trough and its response to ENSO forcing. *Climate Dynamics*, doi: 10.1007/s00382-016-3077-8.

Leung, Y. T. and W. Zhou, 2016: Direct and indirect ENSO modulation of winter temperature over the Asian–Pacific–American region. *Scientific Reports*, doi: 10.1038/srep36356.

Leung, Y. T. and W. Zhou, 2016: Eddy contributions at multiple timescales to the evolution of persistent anomalous East Asian trough. *Climate Dynamics*, doi: 10.1007/s00382-015-2702-2.

Li, X. Z., Y. Q. Chen and W. Zhou, 2016: Response of winter moisture circulation to the India-Burma trough and its modulation by the South Asian waveguide. *J. Climate*, doi: 10.1175/JCLI-D-16-0111.1.

Li, X. Z. and W. Zhou, 2016: Modulation of the interannual variation of the India-Burma Trough on the winter moisture supply over Southwest China. *Climate Dynamics*, **46**, 147-158, doi: 10.1007/s00382-015-2575-4.

Li, X. Z., W. Zhou and Y. Q. Chen, 2016: Detecting the origins of moisture over Southeast China: Seasonal variation and heavy rainfall. *Adv. Atmos. Sci.*, **33**, 319-329.

Liu, K. S. and J. C. L. Chan, 2016: Variations in the power dissipation index in the East Asia region. *Climate Dynamics*, doi 10.1007/s00382-016-3185-5.

Morakinyo, T. E. and Y. F. Lam, 2016: Study of traffic-related pollutant removal from street canyon with trees: dispersion and deposition perspective. *Environmental Science and Pollution Research*, **23**, doi: 10.1007/s11356-016-7322-9.

Morakinyo, T. E. and Y. F. Lam, 2016: Simulation study on the impact of tree-configuration, planting pattern and wind condition on street-canyon's micro-climate and thermal comfort. *Building and Environment*, **103**, 262-275, doi: 10.1016/j.buildenv.2016.04.025.

Morakinyo, T. E., Y. F. Lam and S. Hao, 2016: Evaluating the role of green infrastructures on near-road pollutant dispersion and removal: Modelling and measurement. *Journal of Environmental Management*, **182**, 595-605, doi: 10.1016/j.jenvman.2016.07.077.

Wang, L., W. Chen, W. Zhou and G. Huang, 2016: Teleconnected influence of tropical Northwest Pacific sea surface temperature on interannual variability of autumn precipitation in Southwest China. *Climate Dynamics*, **45**, 2527-2539, doi: 10.1007/s00382-015-2490-8.

Wang, L., G. Huang, W. Zhou and W. Chen, 2016: Historical change and future scenarios of sea level rise in Macau and adjacent waters. *Adv. Atmos. Sci.*, **33**, 462-475, doi: 10.1007/s00376-015-5047-1.

Wang, W. W. and W. Zhou, 2016: Statistical modeling and trend detection of extreme sea level records in the Pearl River Estuary, *Adv. Atmos. Sci.*, **34**, 383-396, doi:10.1007/s00376-016-6041-y.

Wang, W. W., W. Zhou, X. Z. Li, X. Wang and D. X. Wang, 2016: Synoptic-scale characteristics and atmospheric controls of summer heat waves in China. *Climate Dynamics*, doi: 10.1007/s00382-015-2741-8.

Zhou, W., C. Y. Li and C. H. Chow, 2016: Intraseasonal variation of visibility in Hong Kong. *Adv. Atmos. Sci.*, **34**, 26-38, doi:10.1007/s00376-016-6056-4.

Staff list

Director

Prof. Johnny CHAN	Chair Professor of Atmospheric Science

Deputy Director

Dr. Zhi NING	Assistant Professor

Members

Prof. Ronghui HUANG	Honorary Professor (Academician, Chinese Academy of Sciences)
Prof. Chongyin LI	Honorary Professor (Academician, Chinese Academy of Sciences)
Prof. Peter BRIMBLECOMBE	Associate Dean (Research and Postgraduate Studies) Chair Professor of Environmental Chemistry
Dr. Wen ZHOU	Associate Professor
Dr. Nicky LAM	Assistant Professor
Dr. Keith NGAN	Assistant Professor

Advisory Committee

Prof. Yihui DING	Academician, Chinese Academy of Engineering
Lord Prof. Julian HUNT	Professor, University College London, Fellow of Royal Society

Researchers

Appointed by Centre

Dr. Frederick Dane WESTERDAHL	Research Fellow
Dr. Chi Kit TANG	Postdoctoral Fellow
Dr. Junke ZHANG	Postdoctoral Fellow
Mr. Kin Sik LIU	Senior Research Assistant
Mr. Ka Wai NG	Research Assistant
Ms. Li SUN	Research Assistant
Mr. Peng WEI	Research Assistant
Ms. Qian ZHANG	Research Assistant

Guy Carpenter Asia-Pacific Climate Impact Centre
City University of Hong Kong
Tat Chee Avenue, Kowloon,
Hong Kong, China.

Tel: (852) 3442 7359
Email: gcacic@cityu.edu.hk
Website: http://www.cityu.edu.hk/gcacic/

MIX
Paper from responsible sources
FSC™ C102099

Printed on FSC™ Certified Paper with SOY INK